Nano-hardening features in high-dose neutron irradiated Eurofer97 revealed by atom-probe tomography

B. Gómez-Ferrer, C. Dethloff, E. Gaganidze, L. Malerba, C. Hatzoglou, Cristelle Pareige

Journal of Nuclear Materials 537 (2020) 152228

Contents lists available at ScienceDirect

Journal of Nuclear Materials

journal homepage: www.elsevier.com/locate/jnucmat

Nano-hardening features in high-dose neutron irradiated Eurofer97 revealed by atom-probe tomography

B. Gómez-Ferrer [a], C. Dethloff [b], E. Gaganidze [b], L. Malerba [c], C. Hatzoglou [a], C. Pareige [a, *]

[a] Normandie Univ, UNIROUEN, INSA Rouen, CNRS, Groupe de Physique des Matériaux, 76000, Rouen, France
[b] Karlsruhe Institute of Technology, Institute for Applied Materials (IAM), Hermann-von-Helmholtz-Platz 1, 76344, Eggenstein-Leopoldshafen, Germany
[c] Materials of Energy Interest Division, Technology Department, CIEMAT, Avda. Complutense 40, 28040, Madrid, Spain

ARTICLE INFO

Article history:
Received 20 November 2019
Received in revised form
13 April 2020
Accepted 6 May 2020
Available online 14 May 2020

ABSTRACT

High dose (15 and 32 dpa), 300–330 °C neutron irradiated Eurofer97 samples (WTZ, ARBOR-I and SPICE campaigns) have been analysed using atom probe tomography. Segregation of solutes (Si, P, Mn and sometimes Cr and Ni) has been observed at dislocation loops, dislocation lines, grain boundaries and sometimes forming clusters. The decorated objects are extensively surrounded by "Mn clouds". Around the "Mn clouds" a high density population of spherical CrMn-rich clusters which nucleate sometimes at the Cr-rich border of dislocation loops has been revealed. Finally, considering the density and size of (i) decorated DLs, (ii) voids, (iii) CrMn-rich clusters and (iv) precipitates, the increase of the yield stress has been assessed based on a quadratic superposition of Orowan models.

1. Introduction

Eurofer97 (E97) is one of the most technologically developed fusion steels. It will be used in the EU breeding blanket (BB) modules in ITER and is considered as the baseline material choice for EU DEMO reactor designs [1–5]. One of the main problems is the radiation embrittlement at low temperature (250–340 °C) which can compromise the design of some BB and eventually the energetic efficiency and the objective of EU DEMO. Thus, understanding the mechanisms at the origin of this phenomenon is important in order to push reduced activation ferritic-martensitic (RAFM) steels to lower ductile-brittle transition temperatures after irradiation. This work is focused on the understanding of hardening at the origin of the hardening embrittlement, which is believed to be mainly driven by a microstructure composed by dislocation loops, voids and solute clusters (SC).

In the past, three important neutron irradiation campaigns have been carried out by Karlsruhe Institute of Technology (KIT) for the study of the effects of medium and high doses on impact, tensile and low cycle fatigue properties [6] in E97: SPICE [7,8] (15 dpa, 250–450 °C), WTZ 01/577 [9] (15 dpa, 330 °C) and ARBOR-I [10] (32 dpa, 330 °C). So far, the microstructure of these irradiated samples has been extensively characterized by transmission electron microscope (TEM): on the one hand the influence of irradiation on size and density of pre-existing precipitates [11] and on the other the formation of irradiation features such as dislocation loops (DL) and voids [12–15]. All these features can act as obstacles for the dislocation glide and thus account for the increase in yield stress due to irradiation. In the case of the pre-existing precipitates, even though neutron irradiation has been proved to be responsible for a significant carbide growth, the evaluation of the carbide hardening using a simple Dispersed Barrier Hardening (DBH) model was estimated to be negligible [11] when compared to the contributions of the DL [12,13]. To date, the radiation defects visible to the TEM (voids, carbides and DL) have been insufficient to explain the hardening after tensile tests [11,12]. Therefore, it has been postulated that the presence of small objects observed at the resolution limit of TEM, aka "black dots" (BD), could significantly contribute to the total hardening. The nature of these small objects remains, however, still unknown, although based on some preliminary results obtained with atom probe tomography (APT) [16], that reveal the presence of CrMn-rich clusters (enriched up to 20 at% in Cr and 4% in Mn), it has been suggested that the BD could be nano-sized Cr-rich clusters [11].

Meanwhile, work on low-dose neutron irradiated Fe–Cr model alloys, that contained Ni, Si and P impurities, and FM steels, E97 and T91, suggested that the contribution to the yield stress increase from CrNiSiP-rich clusters (henceforth CNSP clusters) and Cr-rich

* Corresponding author.
E-mail address: cristelle.pareige@univ-rouen.fr (C. Pareige).

https://doi.org/10.1016/j.jnucmat.2020.152228
0022-3115/

clusters (sometimes referred to in literature as α' precipitates), both detected by APT, may be very significant [17,18]. The number density and size of these SC, as well as the other irradiation defects, can be used as input to hardening models that work very well for low-dose neutron irradiated alloys [17,18]. The CNSP clusters are believed to result from radiation induced segregation [19,20] on small immobilized [21,22] defect clusters or loops. In contrast, the Cr-rich clusters are believed to be the consequence of phase demixing inside the miscibility gap of the Fe–Cr phase diagram, even though their Cr concentration is often found lower than it should be, possibly due to a combination of dose rate and sink strength effects [23,24], as well as, to a lesser extent, by APT technique limitations [25]).

In order to verify the possible formation of such SC at low-temperature (300–330 °C) in neutron irradiated E97 from the ARBOR, WTZ and SPICE experiments, APT has been used to examine the microstructure of samples from these campaigns. The 3D element maps thereby obtained have been carefully analysed to rationalize the inherent features of the radiation-induced solute redistribution, characterizing the SC that have been identified in terms of radius, density and chemical composition. Finally all microstructural features identified by TEM and APT have been used as input to estimate the corresponding hardening by means of a modified Orowan model [26] (henceforth simply Orowan model).

2. Experimental

2.1. Reference material and irradiation conditions

The studied material is tempered RAFM alloy E97 (nominal composition in wt.% Fe–9Cr – 1.1W–0.2 V – 0.12Ta), supplied by KIT. It corresponds to the heat E83697 and its thermo-mechanical history and nominal composition are carefully described in Ref. [6] and Table 1. Additionally, the concentrations in the grains of E97 in the as-received condition, as obtained by APT in the present work is also presented in Table 1. The description of how the measurements were performed and further details are given in sections 2.3 and 3.1.

The neutron irradiation conditions correspond to three campaigns carried out by KIT: (i) SPICE [7,8] (300 °C, 15 dpa) in the High Flux Reactor (HFR) of NRG in Petten (NL); WTZ 01/577 (330 °C, 15 dpa) [9] and ARBOR-I [10] experiments (330 °C, 32 dpa) in the BOR-60 fast reactor of SSC RIAR in Dimitrovgrad (Russia). The details of the irradiations can be found in Ref. [6] and a summary is reported in Table 2. The chosen conditions allow the evolution with dose to be studied by comparing the microstructures of WTZ (15 dpa) and ARBOR-I (32 dpa), while assessing also the influence of the neutron spectrum, since SPICE specimens where irradiated with a mixed neutron spectrum whereas in WTZ and ARBOR-I the spectra contained only fast neutrons, as is indicated in Table 2. Fast neutrons are not producing He by transmutation after irradiation while thermal neutrons are producing 10.2 atomic parts per million (appm) on SPICE samples, according to the estimations made in Ref. [27], mainly due to their absorption by ^{10}B isotopes.

2.2. Available data

As mentioned, the microstructure of the irradiated samples has been extensively characterized by TEM. Table 2 contains the values of number density and diameter of the so far characterized defect and precipitate populations: DL [12,13,15], voids [12,13], MX carbonitrides and $M_{23}C_6$ carbides [11,13]. In WTZ and ARBOR-I specimens, BD and clearly identifiable DL were counted together and summed up in one density by Weiβ et al. [12] during the TEM investigations. In the case of SPICE specimens it was very difficult to count BD in the TEM micrographs due to contrast issues and thus only clearly visible and identifiable loops where counted [13] and the DL density was calculated using the statistical analysis **g·b** method presented by Prokhodtseva et al. [30] in order to account for the invisible loops. Dethloff et al. [13] also re-calculated the DL densities given by Weiβ [12] using the **g·b** method in order to provide a more accurate value of DL + BD densities for WTZ and ARBOR-I. The values of DL presented in Table 2 and used for the hardening assessment in this work are the values presented in Refs. [13]. Concerning voids, the larger sizes and densities created during SPICE irradiation are probably due to the vacancy stabilizing effect of He. The experimental values of the increase in yield stress are also provided in Table 2.

2.3. Experimental on APT

The E97 (83697) APT samples from ARBOR, SPICE, WTZ and as-received were lifted-out at the Hot Cells facility from Fusion Materials Laboratory of KIT using a SEM-FIB FEI Scios. The samples (2 x 20 × 5 μm^3) were lifted-out from 4 x 3 × 0.2 mm^3 slices already cut out from un-deformed parts of broken KLST-type Charpy specimens and electropolished for TEM characterization. The lift-outs were made in the samples named E104 (ARBOR-I), YA08 (SPICE) and 2E123 (WTZ) and from electropolished regions. Further details on the specimen preparation for TEM analysis can be found in Ref. [11]. Two lift-out of each specimen were made and thus 10-12 pre-tips of each condition were welded on Si micro-coupons. Subsequently the pre-tips underwent FIB annular milling to create APT tips at the GENESIS facility at Groupe de Physique des Matériaux (GPM) in Rouen (France) using a SEM-FIB ZEISS Crossbeam 540. The final milling was performed with a Ga beam energy of 2 kV in order to reduce implantation of Ga ions in the material.

APT acquisitions were made in the GENESIS facility using a Local Electrode Atom Probe (LEAP 4000 XHR) from CAMECA. The samples were set at a temperature of 50K in order to avoid preferential evaporation of Cr atoms. The LEAP has a detector efficiency of 36% and provides a high mass resolution thanks to the presence of a reflectron. During the APT experiments the specimens were electrically pulsed with a pulse fraction of 20% at a pulse repetition rate of 200 kHz. The detection rate was set up between 0.15% and 0.25%. Subsequently the APT volumes were reconstructed using IVAS 3.8.0

Table 1
Composition of E97 (Heat 83697). N: Nominal composition provided in Ref. [6]. M: Matrix composition obtained by APT in this work. Fe in balance.

	C (at%)	Cr (at%)	N (at%)	Si (at%)	P (at%)	Ni (at%)	V (at%)	Ta (at%)
N	0.556	9.55	0.071	0.119	<0.009	0.021	0.218	0.043
M	0.05 ± 0.02	8.7 ± 0.3	0.05 ± 0.04	0.12 ± 0.02	0.006 ± 0.003	0.021 ± 0.006	0.148 ± 0.007	<0.001
	W(at%)	**Mn (at%)**	**Mo (at%)**	**Cu (at%)**	**Ti (at%)**	**Al (at%)**	**Co (at%)**	**B(at%)**
N	0.324	0.476	0.001	0.003	0.010	ND	ND	<0.005
M	0.27 ± 0.02	0.428 ± 0.013	ND	0.002 ± 0.001	ND	0.008 ± 0.004	0.006 ± 0.001	ND

*ND: not detected.

Table 2
Studied irradiation conditions on E97 [6,8–10],estimated generated He [27] after irradiation and determined hardening [28,29].Also density and size of hardening features—DL [12,13,15], voids [12,13], MX carbides and $M_{23}C_6$ carbides [11,13]— as revealed by TEM.

Irradiation campaign	WTZ [9]	SPICE [7,8]	ARBOR-I [10]
Reactor	BOR60	HFR	BOR60
T_{irr} (°C)	330	300	330
Dose (dpa)	15	15	32
Dose rate (dpa/s)	8.04×10^{-7}	2.25×10^{-7}	8.04×10^{-7}
Flux ($m^{-2}s^{-1}$)	1.8×10^{19} (E > 0.1eV)	1.4×10^{18} (thermal) 4.0×10^{18} (E > 0.1eV)	1.8×10^{19} (E > 0.1eV)
Irradiation time (h)	5.200	18.900	11.100
He (appm)	–	10.2	–
Δσ (MPa) (T_{test} = 300 °C)	415	452	514
DL density (m^{-3})	2.0×10^{22}[a] (1.6×10^{22} in Ref. [12])[b]	6.3×10^{21}	2.4×10^{22}[a] (2.2×10^{22} in Ref. [12])[b]
DL mean Ø (nm)	3.4	3.3	4.8
Void density (m^{-3})	3.6×10^{20}	6.3×10^{21}	2.3×10^{21}
Void mean Ø (nm)	2.6	2.3	1.6
MX density (m^{-3})	3.9×10^{19}	3.6×10^{19}	4.2×10^{19}
MX mean Ø (nm)	28.6	27.4	29.0
$M_{23}C_6$ density (m-3)	5.6×10^{19}	4.2×10^{19}	5.5×10^{19}
$M_{23}C_6$ mean Ø (nm)	99.0	91.4	100.0

[a] Values including BD.
[b] Values previously reported by Weiβ et al. [12], including BD, prior to recalculation using the statistical analysis **g·b** method. Previous hardening assessments have been done based on these values.

(CAMECA software). The reconstruction factors have been adjusted for every sample. The compression factor (ξ) has been systematically derived from the crystallographic angles between poles observed on the desorption maps and the field factor (k) has been derived from the expected interplanar distance at the poles. The values used for ξ and k have ranged between 1.57-1.80 and 4.0–5.5 respectively.

The APT data treatment was carried out using the 3D Data Software for Atom Probe Tomography developed by the GPM research group. In order to accurately measure the concentrations, isotopic overlaps, such as $^{54}Cr^{2+}/^{54}Fe^{2+}$, $^{58}Fe^{2+}/^{58}Ni^{2+}$ or $^{31}P^{+}/^{62}Ni^{2+}$, have been taken into account to make the appropriate corrections in the mass spectrum. Two different statistical methods have been used to determine whether the chemical species where randomly distributed in the matrix or not in the as-received condition: (i) For concentrated species, in particular Cr, the Thuvander method [31] has been used and (ii) the 1st Nearest-Neighbour (1NN) method [20,32] was applied to study the distributions of impurities or low-alloying elements (P, Si, Ni, Mn, etc..). The Thuvander method compares the standard error of the experimental distribution to the standard deviation of the binomial distribution corresponding to an homogeneous distribution of the Cr for different sampling volumes. The 1NN statistical tool provides de probability distribution ($P_{X\text{-}Y}$) of finding an element X around an element Y. Comparison of the experimental distribution with the random distribution enables conclusions to be drawn on the randomness of the species distributions.

The main analysis of this work was oriented to study the redistribution of the chemical species after neutron irradiation. For the identification of SC or segregated areas an iso-concentration method (ICM), which has been extensively described elsewhere [20,33,34], has been used. The ICM(X) can be understood as a filter which highlights the regions of the APT volumes where the local concentration of a specific chemical species (X) is over a threshold value. The ICM is based on the choice of three parameters: a concentration threshold (C_{th}), a threshold distance under which an atom pertains to a cluster (d = 0.2 nm) and a minimum number of atoms (N_{min}) of X element which should be present in the cluster, in order to consider it a real cluster and avoid the detection of ghost clusters (i.e. clusters which might be present in a random solid solution simply due to statistics). The study of Cr-rich regions was performed by applying the ICM method on Cr, hereafter named ICM(Cr), with the following criteria: C_{Cr} > ~15 at% N_{min} = 11-20 Cr atoms. Similarly, ICM(SiP) has been applied to identify the regions which are enriched in Si and/or P. In practical terms this means that the filtering is performed as if Si and P atoms were the same element and thus the effective nominal concentration in the sample would be $C_{SiP} = C_{Si} + C_P$. After testing different possibilities, it was concluded that using ICM(SiP) instead of ICM(Si) or ICM(P) separately is the only way to identify all the irradiation features. The parameters used are: C_{SiP} > ~2 at% and N_{min} = 2-7 Si and P atoms.

Spherical clusters highlighted by the ICM(Cr) filter are characterized in terms of number density (N_V), size (radius, R), volume fraction (f_V) and concentration at the core. N_V was determined by the ratio of the number of detected clusters over the analysed volume. The detected clusters, right after application ICM, are often found to be surrounded by a matrix shell rich in Fe, this means that matrix atoms in the vicinity of the clusters are erroneously associated with them. An erosion method was applied to systematically remove such shells before measuring the size and the volume fraction. An accurate description of the erosion method can be found in Ref. [35] section 3.2. The radius of each cluster was calculated as indicated in equation (1), approximating the clusters to a sphere:

$$R_{eq} = \sqrt[3]{\frac{3nV_{at}}{4\pi Q}} \quad (1)$$

with n the number of detected atoms in each cluster, V_{at} the Fe atomic volume ($a_0^3/2$ with a_0 the lattice parameter) and Q the detector efficiency. The radius R is the average of the equivalent radius of every cluster ($R = \langle R_{eq} \rangle$). f_V was calculated by the ratio of the number of atoms inside the clusters to the total number of collected atoms. The cluster's composition was measured at the cluster's core, on the plateau of the erosion concentration profiles [25,36]. The cluster characteristics given by N_V, R, f_V and composition values were averaged over all the APT analysed volumes (at least 3 for each condition).

Whenever solutes decorating dislocation loops were detected instead of sphere-like clusters, linear concentration profiles were

drawn to spot enrichment or depletion of the various species at these defects.

3. Results

3.1. As-received materials

The matrix composition calculated and presented in Table 1 (averaged over 5 different grains) refers to the composition inside the grains excluding grain boundaries (GB) or the pre-existing precipitates. These values are thus the average concentrations on the areas probed by the APT. It is worth noting that the concentrations are given in at.% and that there are differences in Cr, C or P concentrations with respect to the values given by the manufacturer [6] due to the existence of the pre-existing precipitates in the steel ($M_{23}C_6$ or MX carbonitrides [11]) and segregations at the GB that decrease the nominal intragranular concentration of these species. Several $M_{23}C_6$ carbides (M = Fe, Cr, W, V, Mn, B) and some low angle GB that were enriched in Cr, Mn and P were found during analysis. Most P atoms were found at the carbide-matrix interface and at the GB, yet small amounts of P and unexpectedly of Ni where detected inside the grains, as well.

The statistical analysis (Thuvander method and 1NN method) of the distribution of the different chemical species present in the alloy shows that all the elements are randomly distributed on the as-received condition. The results are available on a supplementary information section S1.

3.2. Neutron irradiated materials

The raw reconstructed atom distribution maps for each irradiation condition and each relevant chemical species are shown in Fig. 1. Filtered distribution maps using ICM are provided in Fig. 2 and in the videos: v_WTZ_ICM-SiP, v_WTZ_ICM-Cr, v_SPICE_ICM-SiP, v_SPICE_ICM-Cr, v_ARBOR_ICM-SiP and v_ARBOR_ICM-Cr. These images and videos reveal a very complex and hierarchical microstructure: (i) Cr-rich clusters, (ii) Si, P, Mn and sometimes Ni segregation at dislocation loops or lines or forming isolated clusters, and (iii) Mn clouds. Some other elements such as W or V are placed outside the irradiation features.

Some areas have been highlighted in Fig. 1(a). The area selected by a circle contains the only G-phase particle ($Ni_{16}Si_7Mn_6$) found along this study. The square volume selection is the front view (upper) and top view (lower) where only Si and P atoms are represented in blue. The atom distribution strongly suggests the presence of underlying dislocation loops and lines. These regions can be identified using ICM(SiP).

The regions highlighted after the application of ICM(SiP) are shown in Fig. 2 (columns (1) and (2)). These regions take the shape of small clusters and sometimes the solute spatial distribution reveals the presence of underlying dislocation loops and dislocation lines. The average concentration of the ICM(SiP) highlighted areas and the volume fraction of atoms in these regions are presented in Table 3. The study of the local concentration of these regions reveals that these are not only enriched in P and Si, but also in Ni (despite the little amount of Ni in the matrix most of it is found at the crystal defects), Cr (average 2% increase with respect to the nominal concentration) and Mn. Therefore, from now on, these regions will be referred as to SiPNiMnCr-rich regions. These regions are surrounded by a more extended segregated zone in Mn, hereafter referred to as “Mn clouds”. Concerning the volume fraction of atoms in the segregated zones, no significant differences have been revealed as a function of the irradiation condition (dose or spectrum).

After the analysis of the APT datasets with ICM(Cr) – an example of which can be found in Fig. 2 columns (3) and (4)— two families of Cr-rich objects were identified: (i) CrMn-rich spherical clusters which can be characterized in terms of size, number density and composition and (ii) zones which we call Cr-segregations because of their non-spherical shape and/or their lower Cr content. The very small and the non-spherical clusters considered as Cr-segregations have average compositions of 25 at%Cr – 2 at%Mn (Fe balance). The characteristics of the CrMn spherical clusters are presented in Table 4. The number density ranges from 2.0 to 4.6 $10^{23}m^{-3}$ and the measured average radii range between 1.4 and 1.7 nm. The average core Cr concentration is about 55–65 at%, nevertheless it has been observed that the Cr concentration increases with the size of the clusters.

Further analysis, made by means of linear profiles on some of the CrMn clusters along the Z direction (i.e. the evaporation direction), has been additionally done. The profiles reveal plateaus at maximum values of Cr concentration at the core of the biggest clusters of 80 at% as shown in Fig. 3. The possible deviations in Cr concentration at the clusters due to APT technical limitations (i.e. lateral resolution and local magnification effects due to low evaporation field at the CrMn clusters) were evaluated by Hatzoglou et al. [25] by combining simulations and analytical models. They showed that in the case of a LEAP HR, the dilution of the particles is not larger than 5 at% for 1 nm cluster radius. In the present work the CrMn-rich clusters have been evaluated using the correction model proposed by Hatzoglou et al. [37] which take into account local magnification effects (not the lateral resolution effect). The correction model shows that on average the Cr concentration at the clusters is underestimated by less than 3.5% (see Fig. 4).

Concerning the location of the identified features, the CrMn-rich clusters are not detected at the same places where the SiPNiMnCr-rich regions are found. However both solute rich regions seem to be, in many cases, spatially correlated in a complex way, perhaps connected with underlying loops and definitely connected by the Mn clouds. In the case of WTZ, CrMn-rich clusters are clearly observed at the border or outside the “Mn clouds” and around the dislocation loops (see Fig. 2(a)). An example of this is shown in Fig. 5. The left-hand side in Fig. 5(a) presents a volume selection of the dislocation loop 1, already shown in Fig. 1 (red square), the Cr and Si atoms of the selected volume are plotted in the upper figure and Cr and Mn in the lower figure. It can be clearly seen how the loop is decorated with Si at the inner part, surrounded by Mn and around the loop some CrMn-rich clusters are formed. Fig. 5(b) presents the radiation induced segregation (RIS) profile drawn through the dislocation loop. The profile has been calculated by averaging various linear profiles around the loop (every 30º) avoiding the areas containing CrMn-rich clusters (as indicated by dotted rectangles in Fig. 5(a)). The maximum of Si concentration is observed at a distance of 4–6 nm from the center of the loop. This region is also rich in Ni, Mn and Cr. At the outer part of the loop, at a distance of 7–9 nm from the center, the enrichment in Cr is larger. This measurement is coherent with the presence of Cr-segregations revealed after the application of ICM(Cr). Similar phenomenon of non-homogeneous segregation depending on the solute has been already observed at dislocation lines in neutron irradiated FeCrNiSiP model alloys [38]. Concerning SPICE and ARBOR-I samples, the correlation of the Cr-rich clusters around the dislocation loops is less evident because the loops are less visible. However Cr-enriched regions, in Fig. 2(b) and (c) are also observed surrounding Mn clouds and SiPNiMnCr-rich regions.

It is important to notice that the microstructure described so far is not homogeneous all along the FM steel. An example of such inhomogeneities is shown in Fig. 6 and in the video (v_ARBOR_GB) where three different grains are separated by two low angle grain boundaries (LAGB). For one of the GB, accommodation dislocation

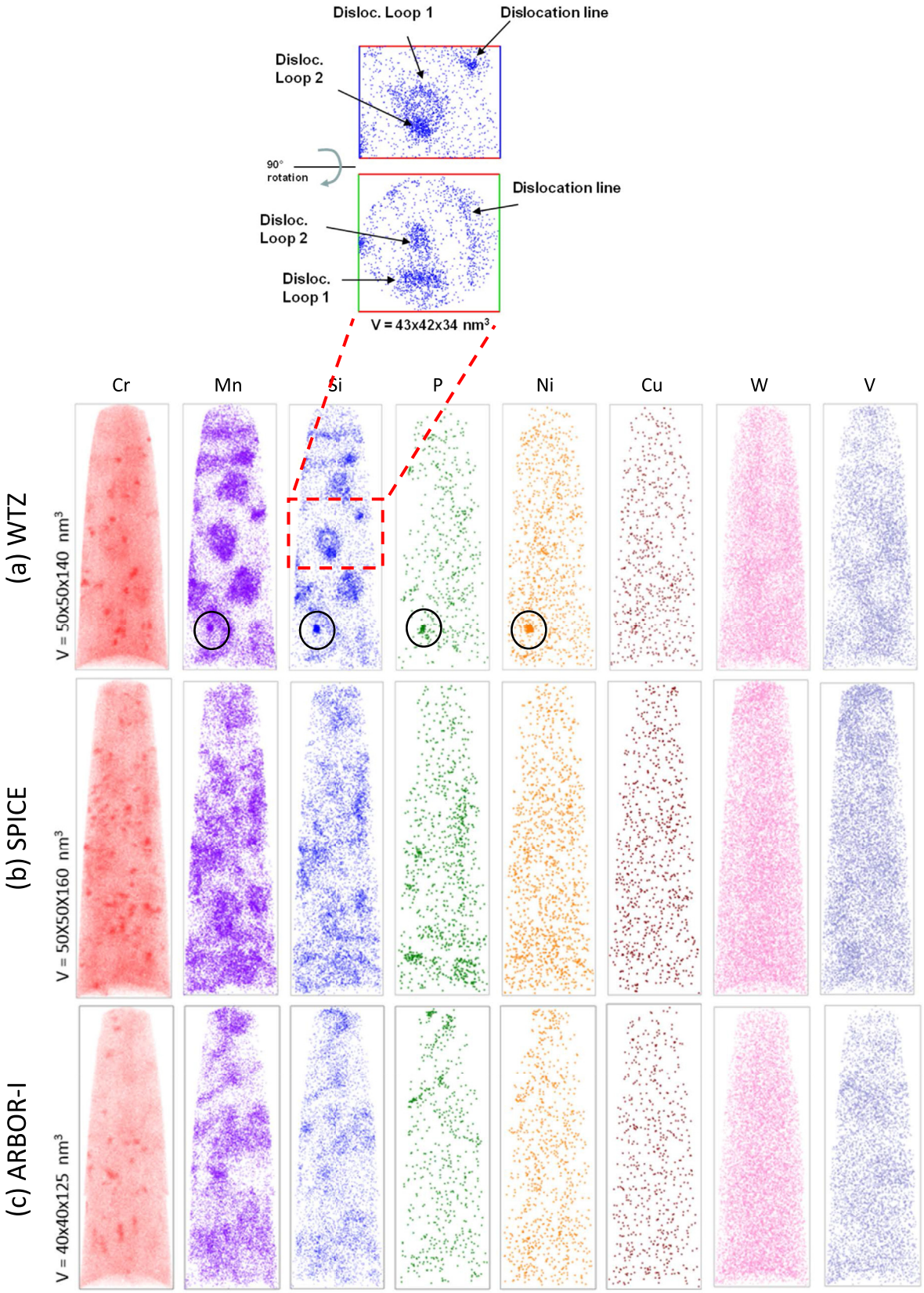

Fig. 1. Atom distribution maps of E97(83697) after neutron irradiations in different conditions: (a) WTZ irradiation - 330 °C - 15 dpa – 8 10^{-7} dpa/s. (b) SPICE irradiation - 330 °C–15 dpa – 2.25 10^{-7} dpa/s. (c) ARBOR irradiation - 300 °C - 32 dpa – 8 10^{-7} dpa/s. The upper part shows a detail of the red framed area on a WTZ specimen, the volume selection corresponds to the red-framed area where only Si and P atoms are represented in blue. (For interpretation of the references to color in this figure legend, the reader is referred to the Web version of this article.)

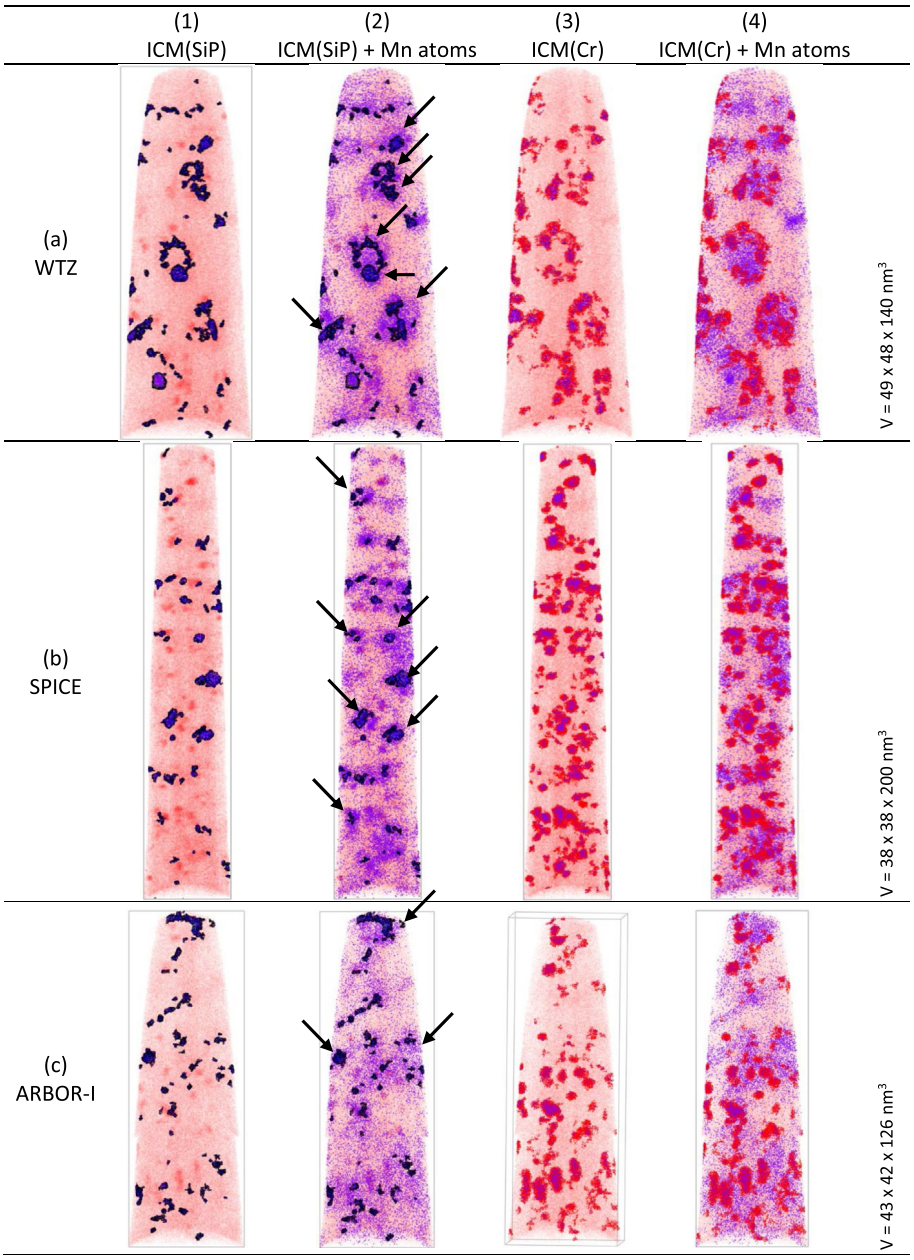

Fig. 2. APT volumes from (a) WTZ, (b) SPICE and (c) ARBOR-I specimens highlighting different features. Column (1): SiP-rich zones highlighted by ICM(SiP) over a background of Cr atoms (in red). Column (2): replica of column (1) showing also all the Mn atoms present in the APT tip. Some zones which are likely to be decorated DL are signed with arrows. Column. (3): Cr-rich zones highlighted by ICM(Cr) over a background of Cr atoms. The red points represent Cr atoms and the purple points represent the Mn atoms present in the Cr-rich regions. Column (4): Replica of column (3) showing also all the Mn atoms present in the APT tip. (For interpretation of the references to color in this figure legend, the reader is referred to the Web version of this article.)

Table 3
Characteristics of the SiPNiMnCr-rich regions revealed by ICM(SiP).

Alloy	Dose (dpa)	f_V (%)	Si (at%)	P (at%)	Cr (at%)	Mn (at%)	Ni (at%)	C (at%)
WTZ	15	0.61 ± 0.13	4.4 ± 0.5	0.24 ± 0.19	11.2 ± 0.7	1.9 ± 0.3	0.8 ± 0.4	0.19 ± 0.10
SPICE	15	0.47 ± 0.15	4.0 ± 0.4	0.4 ± 0.3	11.5 ± 1.8	2.3 ± 0.3	0.8 ± 0.2	0.16 ± 0.08
ARBOR-I	32	0.5 ± 0.2	4.5 ± 0.7	0.4 ± 0.3	11.0 ± 1.0	2.1 ± 0.3	0.7 ± 0.3	0.16 ± 0.13

lines (ADL) revealed by SiMn segregation are visible. A composition profile has been drawn perpendicularly to the ADL (details can be found in the supplementary information Section S2). The profile also reveals a shift between Si, Mn and Cr segregations. Such shift has already been observed in LAGB grain boundaries in FeCr alloys of low purity [38]. CrMn-rich clusters are observed on either side. In the third grain, a depleted zone is observed along the GB. Segregation also occurs at the LAGB indicated on Fig. 6 (Si, Mn, P) but without Cr.

Table 4
Characteristics of the CrMn-rich spherical clusters as measured by APT.

Alloy	Dose (dpa)	f_V (%)	N_V (10^{23} nm^{-3})	R (nm)	Cr (at%)	Mn (at%)	Si (at%)	C (at%)
WTZ	15	0.5 ± 0.3	2.0 ± 1.6	1.7 ± 0.4	61 ± 4	3.6 ± 0.9	0.5 ± 0.4	0.05 ± 0.11
SPICE	15	0.8 ± 0.2	4.6 ± 1.6	1.4 ± 0.4	57 ± 4	3.5 ± 0.9	0.7 ± 0.3	0.13 ± 0.16
ARBOR-I	32	0.5 ± 0.3	2.5 ± 1.5	1.6 ± 0.6	54 ± 4	3.0 ± 2.0	0.6 ± 0.6	0.12 ± 0.16

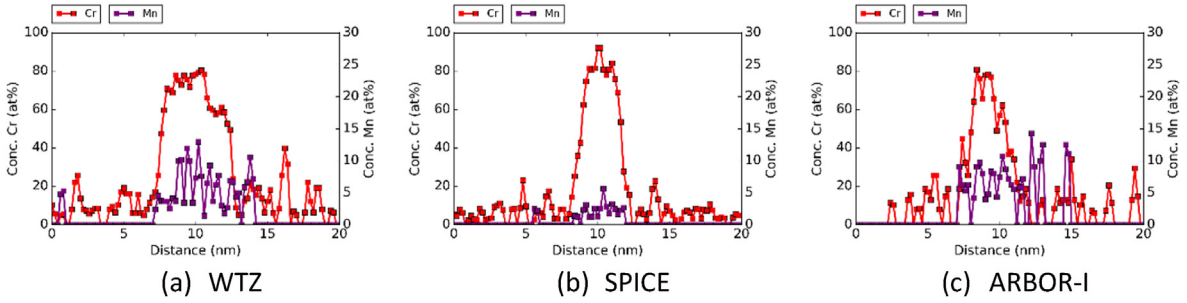

Fig. 3. Linear profiles made along z direction on some of the biggest CrMn clusters found in (a)WTZ, (b) SPICE and (c) ARBOR-I specimens.

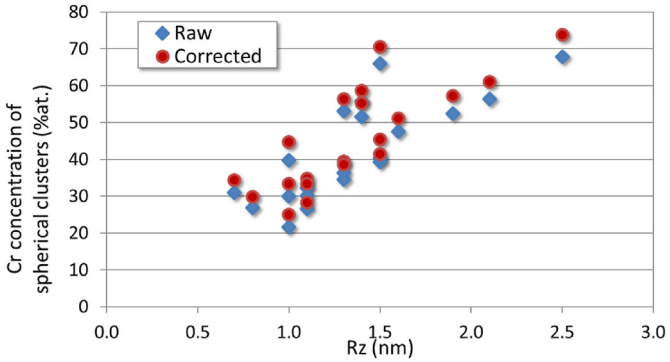

Fig. 4. Raw and corrected values of Cr concentration on CrMn-rich clusters from WTZ specimen. The R_z size indicated on x-axis is the size of the particle along z direction divided by two. Corrected values obtained after application of the Hatzoglou model [37].

4. Discussion

4.1. Irradiation features revealed by APT

At the atomic scale the APT datasets show that, as a consequence of the neutron irradiations, some chemical species have segregated, in particular Si, P, Ni, Mn and Cr. This is not surprising since segregations of these species have been already observed in irradiated ferritic-martensitic steels [20,39–41] and in RPV steels [42–45]. A multiscale approach based on the combination of DFT calculations and a self-consistent mean-field approach has shown that, at 300 °C, P, Si, Ni and Mn can be dragged by migrating vacancies [46–48] and P, Mn and Cr can also be transported via interstitial mechanism [48,49]. The SiPNiMnCr-rich regions are sometimes arranged in such a way that is very clear—namely in WTZ specimens— that they are decorating dislocations loops. In other cases, groups of clusters which seem to decorate a loop are observed (see arrows in Fig. 2). It seems reasonable to assume, when looking at Fig. 4, that in several cases the SiPNiMnCr-rich regions can be decorating TEM-non resolvable DLs and therefore the calculation of loop number density of WTZ and ARBOR-I specimens accounting for the black dots as DL (see Table 2) [12,13] is likely to be accurate. Segregation also occurs at dislocation lines and, in the LAGBs found in ARBOR-I (see Fig. 6). The Mn clouds seem to be placed around the dislocation loops up to their center, as well as along dislocation lines or any other crystallographic defects, and their extension in the space is larger than the features that are identifiable by the isoconcentration tool. The presence of Mn further around the SiPNiMnCr-rich regions at the loops is coherent with the binding trend between solute atoms and DL calculated by Domain and Becquart [22]. This study, by predicting repulsion between V and W atoms and dislocation loops, also agrees very well with the displacement of these atomic species outside the irradiation features, possibly associated with dislocation loops, as is shown in Fig. 1 and quantified in Table 3.

The quasi-spherical clusters rich in Cr and also Mn and Si need a specific discussion, as well. Cr-rich clusters have been reported in many works on electron [50], ion [40,51,52] and neutron irradiations [24,39,53–59]. Typically, a thermodynamic origin is attributed to these objects. In E97 the nominal concentration of Cr, 8.7 ± 0.3 at%, falls exactly at the solubility limit at 300 °C reported by the experimental work of Bergner et al. (8.8 at%) [60] and the value reported by Bachhav et al. (8.9 at%) at 320 °C [55,61], thus it is not clear whether these clusters correspond to thermodynamic-driven phase separation or not. The experimental observations made in this work strongly suggest that the local fluctuations of the Cr concentration can promote the nucleation of these particles: (i) Fig. 5(a)shows Cr clusters nucleating around the DLs, (ii) the RIS profile around a DL plotted in Fig. 5(b) shows that the local concentration of Cr around the loop can increase to average values of ~15 at% and (iii) the Cr-segregations, revealed by ICM(Cr) in Fig. 2, often appear around solute decorated dislocation loops. Previous experimental works on low Cr content alloys (6, 9 and 12 w%) [40,59,62,63] reported Cr segregation at dislocation loops as well and this phenomenon has also been predicted by Metropolis Monte-Carlo [64] and phase field (PF) simulations [65]. Both simulation works [64,65] predicted enrichment of Cr at the outer part of the loops since these are tensile stress regions. PF simulations [65], by considering elastic interactions between point defects and dislocation, not only predict Cr enrichment in the traction (outer) part of the loop but also Cr depletion at the compression (inner) part as it is experimentally observed here. Such a complex behavior of Cr segregations is due to the competition of Cr depletion via vacancy mechanism and enrichment via interstitial dragging. The values of 25 at%Cr found in the Cr segregated regions in

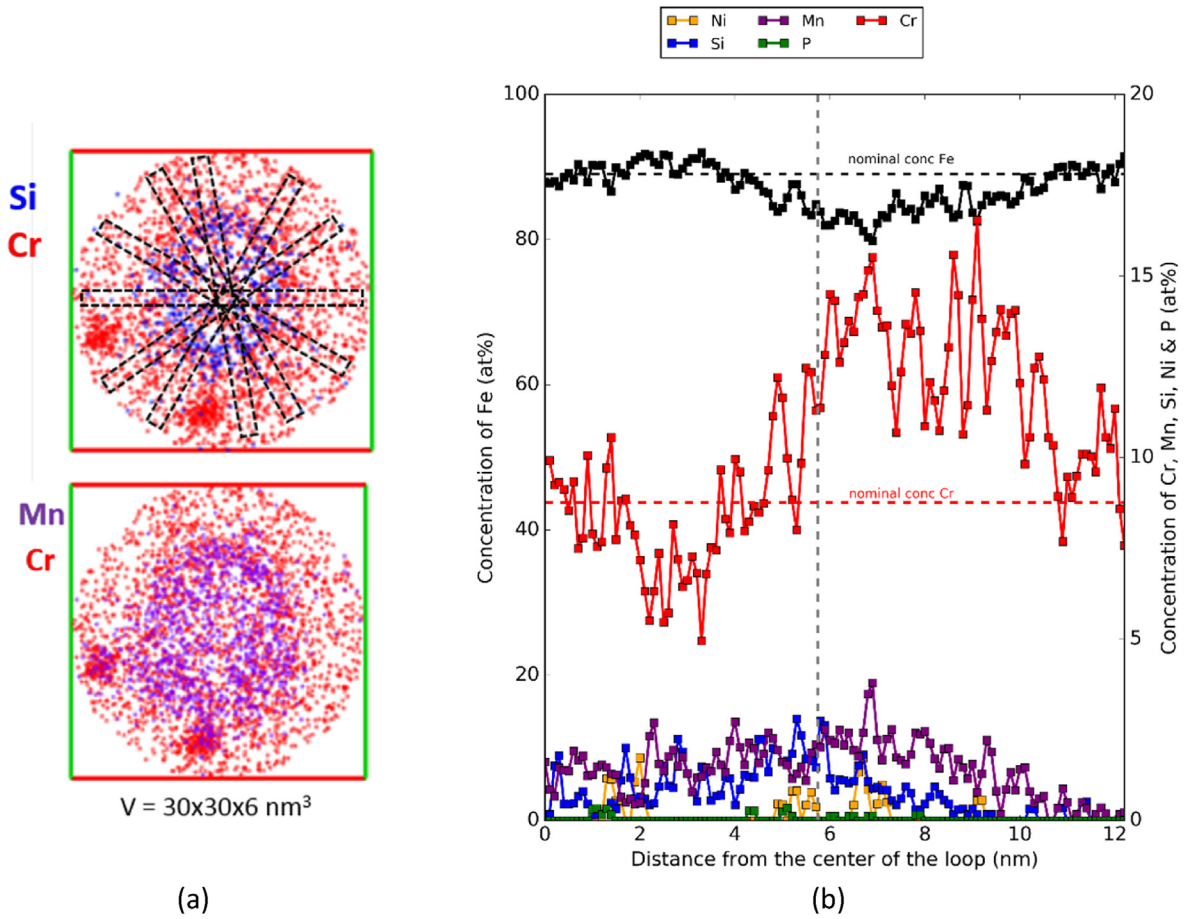

Fig. 5. (a) Atomic maps of Cr and Si (upper figure) and Cr and Mn (lower figure) of an APT sub volume where a dislocation loop has been selected. (b) RIS profile of the selected loop experimentally measured by averaging over several radial concentration profiles. The CrMn-rich clusters have not been taken into account to calculate the RIS profile. Zero represents the center of the loop and the dotted vertical line is presumably the emplacement of the dislocation loop.

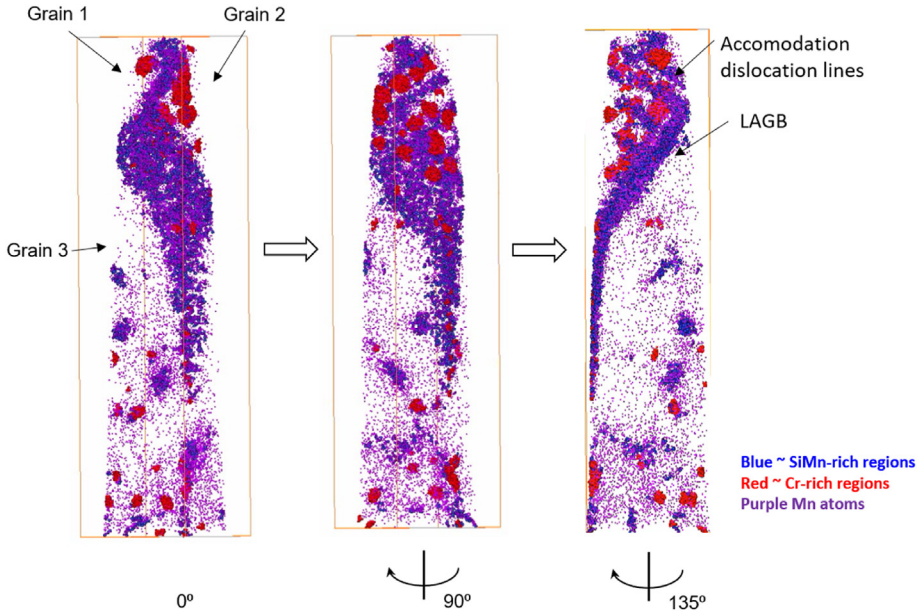

Fig. 6. Different views from an ARBOR APT volume ($36 \times 36 \times 146$ nm^3) exhibiting the intersection between a LAGB and accommodation dislocation lines. Blue dots represent SiMn-rich regions, purple points are Mn atoms and red regions represent CrMn-rich clusters. (For interpretation of the references to color in this figure legend, the reader is referred to the Web version of this article.)

E97 qualitatively match with the values of enrichment measured at DL by Bhattacharya et al. [63] and reported by Zhurkin (of 30 at%) [64]. This match reinforces the idea that Cr-segregations occur around DL. Such local fluctuations of Cr concentration would hence have a radiation induced origin but could nonetheless allow locally the thermodynamic-driven separation between Cr-rich and Fe-rich phases when local Cr concentration exceed the solubility limit, leading to the nucleation of CrMn-rich clusters, which will be therefore considered as α′ particles with Mn. However, the average Cr concentration at the core of the clusters is below the equilibrium concentration predicted by the binary phase diagram. The biggest CrMn-rich clusters, of about ~2 nm in radius, do reach Cr concentration values of 80 at% (as shown in Fig. 3). These values, whose underestimation due to APT limitations is not larger than 3.5 at% (as discussed in section 3.2) [25,37], are coherent with the values reported on neutron irradiation FeCr alloys at 1.8 dpa [62] and by the model presented by Ke et al. [61] at 10 dpa. According to Ke et al. at the steady state the α' Cr concentration is not larger than 83 at% for damage rates of 10^{-7} dpa/s due to cascade mixing, thus they are in line with expectations. Still, in the studied samples, the presence of other—smaller and more diluted—clusters diminishes the average Cr concentration values to 54–61 at%. These values for the average concentration are closer to the reported values in an Fe–9%Cr alloy at 0.6 dpa [39], Fe–10%Cr at 1 dpa [56] and a Fe–10%Cr–10%Al at 7 dpa [54]. The CrMn-rich clusters detected here present a direct positive correlation between their size and their Cr concentration at the core (see Fig. 4). Such correlation with the size for a given dose was also reported by Chen et al. in neutron-irradiated FeCr model alloys [56], but it is not observed in the case of thermal ageing or electron irradiation [50,66], where for any given ageing time or dose the cluster composition is not dependent on the size. However even in those cases the Cr concentration increases with ageing time or dose (the whole Cr concentration distribution shift towards higher values). In this work, after the application of the correction model by Hatzoglou et al. [35] it has been verified that such dependence of the Cr concentration with the cluster size is not an effect related to local magnification effects of the APT technique. Since the irradiations doses and irradiation times are large and we do not observe major difference between 15 dpa and 32 dpa, it is very likely that the Cr composition of the clusters will not further evolve with dose. Thus, the steady state in composition is expected to have been reached and so the origin of this size dependence of the Cr concentration remains unexplained.

The CrMn-rich clusters are found at the border or outside the Mn-clouds which surround most crystallographic defects. They are not associated with decorated dislocation lines, except in the case of the dislocation lines associated with the low angle boundary in Fig. 6 and Fig. SI 4, which show the presence of well-arranged CrMn-rich clusters around the ADL, suggesting that their presence could also enhance the nucleation of the clusters. Such phenomena has been simulated by Thuinet et al. in Fe–9%Cr at 290 °C [65]. The authors showed that local Cr enrichment may be observed near sinks because of flux coupling between Cr and point defects. These enrichments when exceeding the solubility limit, lead to radiation induced precipitation.

In general, no major differences have been found among WTZ, ARBOR-I and SPICE samples, apart from a larger number density of CrMn-rich clusters (and voids, observed by TEM) in SPICE experiments. The SiPNiMnCr-rich regions exhibit the same average solute enrichment in the three conditions and similar f_v within the error bars. However it is worth noting that the identification of DL and dislocation lines by the solutes decoration is much more evident in WTZ samples, followed by ARBOR-I samples whereas the distribution of the enriched areas revealed by ICM(SiP) and ICM(Cr) is more fine and dispersed in SPICE samples.

4.2. Hardening assessment

The neutron irradiations of WTZ, SPICE and ARBOR-I campaigns have produced an increase of the yield stress of several hundreds of MPa (the data are given in Table 2). So far, attempts to correlate the microstructural changes due to irradiation with the change in the mechanical properties where made by applying a DBH model [11,12]. The obstacles considered for previous hardening assessments have been randomly distributed dislocation loops, voids and pre-existing precipitates. Thanks to the microstructural features revealed by APT it is now possible to add the population of CrMn-rich clusters as an additional source of strengthening, treating them as what in previous work has been called α' precipitates [4,5,10]. Moreover, it has been shown how the dislocation loops are decorated with Si, Mn, Cr, Ni and P and the black dots are presumably also small decorated dislocation loops. G-phase precipitates have been detected, but with an extremely low density (only one small particle, shown in Fig. 1(a)), therefore it will not be considered in the assessment.

In this work we therefore extend the DBH approach used in Refs. [11,12] to evaluate the contribution of the CrMn-rich clusters to the increase in the yield strength of E97. The DBH model estimates the critical resolved shear stress (CRSS) of a particular population of randomly distributed non-shearable obstacles using the Orowan model [26]:

$$\tau_{abs} = \alpha_{obs}\, \mu b \sqrt{N_{obs} d_{obs}} \tag{1}$$

where α_{obs} is the obstacle strength, while N_{obs} and d_{obs} are number density and diameter of the obstacles, respectively. The parameter μ is the shear modulus of iron and b is the Burgers vector along the closed-packed direction, which is <111> in the case of bcc ($\sqrt{3}a_0/2$, where a_0 is the lattice parameter). The corresponding yield stress increase, $\Delta\sigma_{obs}$, is then deduced by multiplying the CRSS by the Taylor factor, M (in this work, the value used is 3.06[1] for ferritic steels [17]): $\Delta\sigma_{obs} = M \times \tau_{obs}$. The total increase in the yield stress, due to all defect populations, is obtained by means of a quadratic superposition law:

$$\Delta\sigma_{ys} = \sqrt{\sum_i \Delta\sigma_i^2} \tag{2}$$

with i accounting for the different obstacles: p (pre-existing precipitates, i.e. carbides), v (voids), DL (strongly decorated dislocation loops + black dots) and α' (CrMn-rich clusters).

Since the growth of the pre-existing precipitates (MX and $M_{23}C_6$) is similar in WTZ, SPICE and ARBOR (see Table 2) we have adopted in all conditions the value of $\Delta\sigma_p$ = 19 MPa given in Ref. [11] (for ARBOR).

The calculations of the CRSS for voids, DL and α′ were made applying equation (1). The shear modulus, μ, and the lattice parameter, a_0, were taken from Fe–10%Cr model alloys at a temperature of 300 °C: their values are 75.3 GPa [67] and 2.88 Å [68], respectively. Concerning the obstacle strengths, these are indeed the known unknowns which are typically deduced by fitting the experimental data to the hardening model used. Voids are non-shearable obstacles with α_v = 1 but the values of the obstacle strengths are below 1 in the cases of DL and α'. In this work, different sets of values for the obstacle strengths (summarized in

[1] The authors chose this value for consistency with previous assessments. However, the Taylor factor should be lower due to the activation of at least 12 additional slip systems (the {112} planes) in bcc system.

Table 5) have been used:

(i) On the one hand values have been taken from previous works. In the case of DL the value $\alpha_{DL} = 0.6$ [69] has been maintained, in order to effectively compare with previous assessments [11,12]. Concerning the CrMn-rich precipitates the value $\alpha_{\alpha'} = 0.03$ [17] obtained in Fe–Cr model alloys of low purity has been considered. The results of the prediction in the increase in yield stress obtained using these values are plotted in Fig. 7 (green circles) against the experimental values (squares).

(ii) On the other hand, a least square fit of the obstacle's strength has been made, to fit the experimental values of the increase in the yield strength from WTZ, SPICE and ARBOR irradiation campaigns. The values resulting from this fit are $\alpha_{DL} = 0.68$ and $\alpha_{\alpha'} = 0.17$. The results of the prediction of the increase in the yield strength are plotted also in Fig. 7 (blue stars).

Fig. 7 shows that the least square fitting of the obstacle's strengths, which is giving larger α values for both α_{DL} and $\alpha_{\alpha'}$, is providing a good fit of the experimental data. The values of $\alpha_{\alpha'} = 0.03$ taken from literature [17] does not enable to adjust experimental data. This can be due either to an underestimation of the hardening due to CrMn-rich clusters or to the fact that another ingredient is missing in the calculation of the yield stress increase. An obstacle strength of 0.17 for the α' particles provides a good estimate of the hardening for all three experimental conditions. This strength is 6 times as high as the value fitted in Ref. [17]; however it must be considered that, in this case the particles are bigger which is consistent with a higher value of the obstacle strength. Also, while in the case of reference [17] the obstacles were unambiguously α' precipitates (in model Fe–Cr alloys), here the obstacles are complex structures that are often likely to be associated with Mn clouds (Fig. 2). It is thus very likely that behind the strong strength attributed to α' clusters, there are several contributions: the one of CrMn-rich clusters and a hardening by local solute enrichment due to the redistribution of the chemical elements as Mn clouds, V and W (Fig. 1). Anyhow, consistently with [17], the strength associated to the CrMn-rich clusters is significantly lower than the strength of (decorated) DL. The estimated obstacle strength for DL is also higher than the value previously used. The fact of considering small defects such as DL or BD as strong obstacles must be related to the existence of solute decoration, as revealed by the present work and as previously assessed by simulations [70,71]; otherwise, small undecorated loops would be easily absorbed by dislocation lines, with lower strengthening effect [72,73].

The relative contributions of the different populations of obstacles obtained by applying the presented model after fitting α_{DL} and $\alpha_{\alpha'}$ are depicted in Fig. 8. According to the model used, the contributions to the yield stress increase of DL and chemical features (CrMn clusters, Mn clouds …) are comparable. When the number density and size of the voids becomes larger (SPICE experiment) the contribution of voids starts to be important, as well. Interestingly, the differences in voids density (one order of magnitude higher in SPICE) and CrMn-rich clusters (double in the case of SPICE) are enough to account for the increase in yield strength. Concerning the recalculation of the number densities of DL of ARBOR-I and WTZ specimens made by C. Dethloff [13], it results in a small increase on the density of (DL + BD) and therefore a small increase of the DL relative contribution, $\Delta\sigma_{DL}$, at 15 and

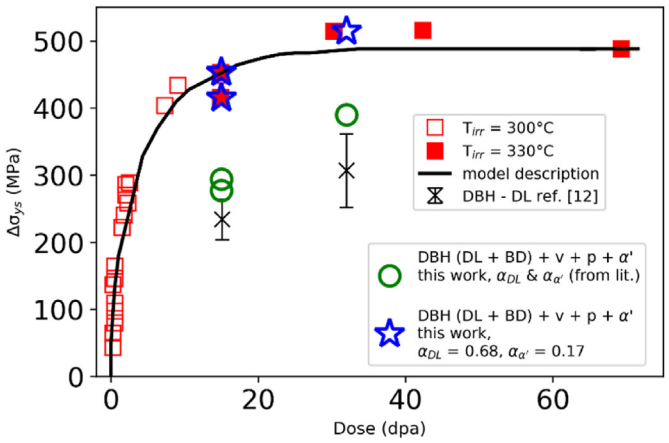

Fig. 7. E97 yield stress increase as a function of neutron irradiation dose at 300–330 °C. The squares (empty and full) are experimental data points from Ref. [6,12]. The continuum line is a description according to the model of Whapham and Makin [28,72]. The black crosses are the results of the hardening assessment published in Refs. [12] accounting for DL + BD (WTZ and ARBOR). The green circles are the results obtained in the present work after applying DBH model using obstacle strengths from other works. The blue stars are the results obtained in the present work after fitting the values of the obstacle strengths for DL (i.e. DL + BD, only DL in SPICE) and α' particles (or CrMn-rich clusters).

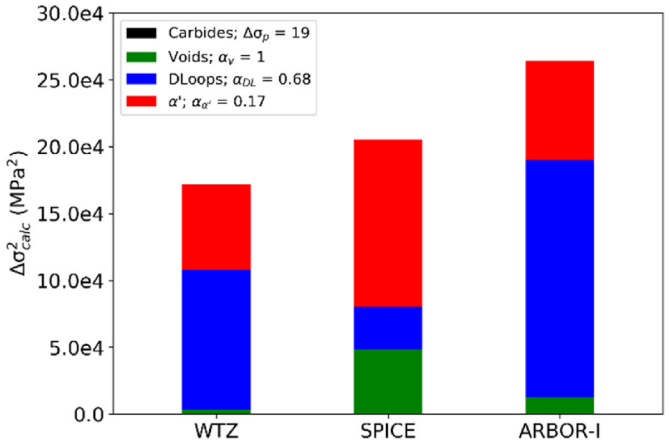

Fig. 8. Calculated versus measured yield stress increase of WTZ, SPICE and ARBOR specimens. The weight of the partial contribution of every defect population is indicated in different colors: black for the precipitates, green for the voids, blue for the DL + BD (only DL for SPICE) and red for the α' particles.

Table 5
Different sets of obstacle strengths (for DL and α') used to assess the impact of the CrMn-rich clusters on the increase in the yield stress according to DBH model.

Source of parameters		Obstacle strengths	
		α_{DL}	$\alpha_{\alpha'}$
Data from literature		0.6 [69]	0.03 [17]
Least squares fit in this work	WTZ & ARBOR[a]	0.682	0.169
	WTZ, SPICE & ARBOR	0.684	0.168

[a] *SPICE not included in the fit since the BD were not quantified.*

32 MPa respectively, in comparison to the values reported by O. Weiβ [12].

The fit values of the obstacle strengths should not be taken at face value, because the hardening model used here is very simple and the features of the defect populations have been deliberately simplified into a very schematic classification. It would be preposterous to expect that this model can accurately reflect the behavior of such a complex microstructure as the one revealed by the high-dose neutron-irradiated E97. However, the current investigation allowed the identification of additional defect populations, the contribution of which is instrumental in order to rationalize the origin of radiation-hardening in E97, and probably other FM steels as well, thereby resolving the aporia that remained from the assessment attempted in Ref. [12]. A more refined assessment of the increase on the yield stress should be addressed by simulations and by the application of more recent models, which could account for the finite strength of the obstacles (e.g. BKS modified model developed by Monnet [73–75]) and the complex microstructure revealed in this work.

5. Conclusions

APT investigations allowed strong solute segregation to be revealed on dislocation loops, lines, GB and clusters and to identify CrMn-rich clusters as additional hardening features. Here is a brief summary of the main observations:

(i) Very strong segregation of different solutes Si, P, Ni, Mn and Cr at dislocation lines, dislocation loops and sometimes forming isolated clusters has been observed in high dose neutron irradiated E97 (15–32 dpa). The involved atomic species do not segregate exactly at the same places, instead they do so according to a sort of nested structure, where Si and P tend to gather at the inner parts of the loops, whereas Cr segregates at the outer parts of the loops, while Mn segregation expands from the core of the crystallographic defects towards the matrix over larges distances, creating “Mn clouds”. Some of these segregated regions could be associated with non-resolvable dislocation loops or black dots, although only in a few cases. In order to fully prove this point, correlative microscopy experiments should be carried out.

(ii) A new, high density (2.0–4.6 $10^{23}m^{-3}$) population of CrMn-rich spherical clusters has been revealed. The mechanisms underlying their formation is most likely radiation-induced precipitation. The direct correlation between size and concentration found for these clusters remains still unexplained. Additionally, the CrMn-rich clusters have been characterized in terms of number density and size in order to introduce these features in a hardening model.

(iii) The stoichiometric G-phase ($Ni_{16}Si_7Mn_6$) was found, but with extremely low density (only one particle in all the APT experiments), thus it is not considered to have any impact on the hardening of neutron irradiated E97.

The hardening assessment made by Weiβ [12] and Dethloff [11] has been completed by introducing a new population of defects revealed by APT, the CrMn-rich clusters. The inclusion of these features together with the fitting of the obstacle strengths of the dislocation loops ($\alpha_{DL} = 0.68$) and the α' particles ($\alpha_{\alpha'} = 0.17$) provides a more accurate estimate of the increase in yield stress than in previous work [11,12]. It is very likely that behind the strong strength attributed to CrMn-rich clusters, there are several contributions: the one of CrMn-rich clusters and the redistribution of the chemical elements as Mn clouds, V and W. According to the model used, DL and the redistribution of chemical species (CrMn-rich particles, Mn clouds …) are the main contributors, with about equal weight, to the total yield stress increase; voids start to play a role when reaching high densities and large sizes, as in the case of the SPICE specimens.

Declaration of competing interest

The authors declare that they have no known competing financial interests or personal relationships that could have appeared to influence the work reported in this paper.

CRediT authorship contribution statement

B. Gómez-Ferrer: Conceptualization, Methodology, Formal analysis, Validation, Investigation, Writing - original draft. **C. Dethloff:** Conceptualization, Validation, Resources. **E. Gaganidze:** Conceptualization, Validation. **L. Malerba:** Conceptualization, Validation, Writing - review & editing, Project administration, Funding acquisition. **C. Hatzoglou:** Formal analysis. **C. Pareige:** Conceptualization, Methodology, Validation, Resources, Writing - review & editing, Supervision, Funding acquisition.

Acknowledgements

This work has been carried out within the framework of the EUROfusion Consortium and has received funding from the Euratom research and training programme 2014–2018 and 2019–2020 under grant agreement No 633053. The views and opinions expressed herein do not necessarily reflect those of the European Commission.

Experiments were performed on the GENESIS platform. GENESIS is supported by the Région Haute-Normandie, the Métropole Rouen Normandie, the CNRS via LABEX EMC and the French National Research Agency as a part of the program “Investissements d’avenir” with the reference ANR-11-EQPX-0020.

To A. Etienne and other PCRs, engineers and technical assistants which made possible the work on GENESIS facility. To H.-C. Schneider and all the team of the hot cell facility in KIT which assisted to the sample lift-out from active E97.

Data Availability

Readers interested on the raw/processed data required to reproduce these findings are invited to contact the authors.

Appendix A. Supplementary data

Supplementary data to this article can be found online at https://doi.org/10.1016/j.jnucmat.2020.152228.

References

[1] D. Stork, P. Agostini, J.-L. Boutard, D. Buckthorpe, E. Diegele, S.L. Dudarev, C. English, G. Federici, M.R. Gilbert, S. Gonzalez, A. Ibarra, C. Linsmeier, A.L. Puma, G. Marbach, L.W. Packer, B. Raj, M. Rieth, M.Q. Tran, D.J. Ward, S.J. Zinkle, Materials R&D for a timely DEMO: key findings and recommendations of the EU roadmap materials assessment group, Fusion Eng. Des. 89 (2014) 1586–1594, https://doi.org/10.1016/j.fusengdes.2013.11.007.

[2] D. Stork, et al., Assessment of the EU R&D Programme on DEMO Structural and High-Heat Flux Materials, 2012.

[3] M.J. Gorley, Critical Assessment 12: prospects for reduced activation steel for fusion plant, Mater. Sci. Technol. 31 (2015) 975–980, https://doi.org/10.1179/1743284714Y.0000000732.

[4] M. Zmitko, Y. Carin, N. Thomas, M. Simon-Perret, A. LiPuma, L. Forest, J. Tosi, G. Aiello, L. Cogneau, J. Rey, H. Neuberger, J. Aktaa, E. Gaganidze, K. Zhang, N. Pierredon, Y. Lejeail, P. Lamagnere, Y. Poitevin, The European ITER Test Blanket Modules: EUROFER97 material and TBM’s fabrication technologies

development and qualification, Fusion Eng. Des. 124 (2017) 767–773, https://doi.org/10.1016/j.fusengdes.2017.04.051.
[5] M. Gorley, E. Diegele, S. Dudarev, G. Pintsuk, Materials engineering and design for fusion—towards DEMO design criteria, Fusion Eng. Des. (2018), https://doi.org/10.1016/j.fusengdes.2018.02.012.
[6] E. Gaganidze, J. Aktaa, Assessment of neutron irradiation effects on RAFM steels, Fusion Eng. Des. 88 (2013) 118–128, https://doi.org/10.1016/j.fusengdes.2012.11.020.
[7] E. Gaganidze, B. Dafferner, H. Ries, R. Rolli, H.C. Schneider, J. Aktaa, Irradiation programme HFR phase IIb - SPICE. Impact testing on up to 16.3 dpa irradiated RAFM steels, Final report for task TW2-TTMS 001b-D05, Karlsruhe, FZKA-7371, https://doi.org/10.5445/IR/270071588, 2008.
[8] E. Materna-Morris, A. Möslang, R. Rolli, H.-C. Schneider, Effect of helium on tensile properties and microstructure in 9%Cr–WVTa–steel after neutron irradiation up to 15dpa between 250 and 450°C, J. Nucl. Mater. 386–388 (2009) 422–425, https://doi.org/10.1016/j.jnucmat.2008.12.157.
[9] C. Petersen, J. Aktaa, E. Diegele, E. Gaganidze, R. Lässer, E. Lucon, E. Materna-Morris, A. Möslang, A. Povstyanko, J. Rensman, B. van der Schaaf, H.-C. Schneider, Mechanical properties of reduced activation ferritic/martensitic steels after European reactor irradiations, in: 21st IAEA Fusion Energy Conference, Chengdu, China, October 16-21, 2006.
[10] C. Petersen, Post Irradiation Examination of RAF/M Steels after Fast Reactor Irradiation up to 33 Dpa and <340°C (ARBOR 1, Karlsruhe Institut of Technologie, 2010. FZKA-7517, https://publikationen.bibliothek.kit.edu/270081166. (Accessed 18 February 2019).
[11] C. Dethloff, E. Gaganidze, J. Aktaa, Quantitative TEM analysis of precipitation and grain boundary segregation in neutron irradiated EUROFER 97, J. Nucl. Mater. 454 (2014) 323–331, https://doi.org/10.1016/j.jnucmat.2014.07.078.
[12] O.J. Weiß, E. Gaganidze, J. Aktaa, Quantitative characterization of microstructural defects in up to 32dpa neutron irradiated EUROFER97, J. Nucl. Mater. 426 (2012) 52–58, https://doi.org/10.1016/j.jnucmat.2012.03.027.
[13] C. Dethloff, E. Gaganidze, J. Aktaa, Microstructural defects in EUROFER 97 after different neutron irradiation conditions, Nucl. Mater. Energy. (2016), https://doi.org/10.1016/j.nme.2016.05.009.
[14] M. Klimenkov, E. Materna-Morris, A. Möslang, Characterization of radiation induced defects in EUROFER 97 after neutron irradiation, J. Nucl. Mater. 417 (2011) 124–126, https://doi.org/10.1016/j.jnucmat.2010.12.261.
[15] C. Dethloff, E. Gaganidze, J. Aktaa, Review and critical assessment of dislocation loop analyses on EUROFER 97, Nucl. Mater. Energy. 15 (2018) 23–26, https://doi.org/10.1016/j.nme.2018.05.015.
[16] S.V. Rogozhkin, A.A. Nikitin, A.A. Aleev, A.B. Germanov, A.G. Zaluzhnyi, Atom probe study of radiation induced precipitates in Eurofer97 Ferritic-Martensitic steel irradiated in BOR-60 reactor, Inorg. Mater. Appl. Res. 4 (2013) 112–118, https://doi.org/10.1134/S2075113313020160.
[17] F. Bergner, C. Pareige, M. Hernández-Mayoral, L. Malerba, C. Heintze, Application of a three-feature dispersed-barrier hardening model to neutron-irradiated Fe–Cr model alloys, J. Nucl. Mater. 448 (2014) 96–102, https://doi.org/10.1016/j.jnucmat.2014.01.024.
[18] G. Monnet, Multiscale modeling of irradiation hardening: application to important nuclear materials, J. Nucl. Mater. 508 (2018) 609–627, https://doi.org/10.1016/j.jnucmat.2018.06.020.
[19] C. Pareige, V. Kuksenko, P. Pareige, Behaviour of P, Si, Ni impurities and Cr in self ion irradiated Fe–Cr alloys – comparison to neutron irradiation, J. Nucl. Mater. 456 (2015) 471–476, https://doi.org/10.1016/j.jnucmat.2014.10.024.
[20] B. Gómez-Ferrer, C. Heintze, C. Pareige, On the role of Ni, Si and P on the nanostructural evolution of FeCr alloys under irradiation, J. Nucl. Mater. Accept. Publ. (2018).
[21] D. Terentyev, M. Klimenkov, L. Malerba, Confinement of motion of interstitial clusters and dislocation loops in BCC Fe–Cr alloys, J. Nucl. Mater. 393 (2009) 30–35, https://doi.org/10.1016/j.jnucmat.2009.05.002.
[22] C. Domain, C.S. Becquart, Solute – ⟨111⟩ interstitial loop interaction in α-Fe: a DFT study, J. Nucl. Mater. 499 (2018) 582–594, https://doi.org/10.1016/j.jnucmat.2017.10.070.
[23] F. Soisson, T. Jourdan, Radiation-accelerated precipitation in Fe?Cr alloys, Acta Mater. 103 (2016) 870–881, https://doi.org/10.1016/j.actamat.2015.11.001.
[24] E.R. Reese, N. Almirall, T. Yamamoto, S. Tumey, G. Robert Odette, E.A. Marquis, Dose rate dependence of Cr precipitation in an ion-irradiated Fe 18Cr alloy, Scripta Mater. 146 (2018) 213–217, https://doi.org/10.1016/j.scriptamat.2017.11.040.
[25] C. Hatzoglou, B. Radiguet, G. Da Costa, P. Pareige, M. Roussel, M. Hernandez-Mayoral, C. Pareige, Quantification of APT physical limitations on chemical composition of precipitates in Fe–Cr alloys, J. Nucl. Mater. 522 (2019) 64–73, https://doi.org/10.1016/j.jnucmat.2019.05.022.
[26] A.K. Seeger, ON the theory OF radiation damage and radiation hardening. https://www.osti.gov/servlets/purl/4280209, 1959.
[27] C. Dethloff, E. Gaganidze, V.V. Svetukhin, J. Aktaa, Modeling of helium bubble nucleation and growth in neutron irradiated boron doped RAFM steels, J. Nucl. Mater. 426 (2012) 287–297, https://doi.org/10.1016/j.jnucmat.2011.12.025.
[28] E. Gaganidze, C. Petersen, E. Materna-Morris, C. Dethloff, O.J. Weiß, J. Aktaa, A. Povstyanko, A. Fedoseev, O. Makarov, V. Prokhorov, Mechanical properties and TEM examination of RAFM steels irradiated up to 70dpa in BOR-60, J. Nucl. Mater. 417 (2011) 93–98, https://doi.org/10.1016/j.jnucmat.2010.12.047.
[29] L. Malerba, C. Dethloff, E. Gaganidze, B. Gómez-Ferrer, M. Konstantinovic, C. Pareige, D1: Summary of Available Data on Selected Materials and Characterization Plan, CfP-AWP17-ENR-LPP-EMR-KLS-05, EUROfusion, 2018.
[30] A. Prokhodtseva, B. Décamps, A. Ramar, R. Schäublin, Impact of He and Cr on defect accumulation in ion-irradiated ultrahigh-purity Fe(Cr) alloys, Acta Mater. 61 (2013) 6958–6971, https://doi.org/10.1016/j.actamat.2013.08.007.
[31] M. Thuvander, H.-O. Andrén, K. Stiller, Q.-H. Hu, A statistical method to detect ordering and phase separation by APFIM, Ultramicroscopy 73 (1998) 279–285, https://doi.org/10.1016/S0304-3991(97)00168-X.
[32] T. Philippe, F. De Geuser, S. Duguay, W. Lefebvre, O. Cojocaru-Mirédin, G. Da Costa, D. Blavette, Clustering and nearest neighbour distances in atom-probe tomography, Ultramicroscopy 109 (2009) 1304–1309, https://doi.org/10.1016/j.ultramic.2009.06.007.
[33] W. Lefebvre-Ulrikson (Ed.), Atom Probe Tomography: Put Theory into Practice, Academic Press, London, 2016.
[34] J.M. Hyde, G. DaCosta, C. Hatzoglou, H. Weekes, B. Radiguet, P.D. Styman, F. Vurpillot, C. Pareige, A. Etienne, G. Bonny, N. Castin, L. Malerba, P. Pareige, Analysis of radiation damage in light water reactors: comparison of cluster Analysis methods for the analysis of atom probe data, Microsc. Microanal. (2017) 1–10, https://doi.org/10.1017/S1431927616012678.
[35] C. Hatzoglou, B. Radiguet, P. Pareige, Experimental artefacts occurring during atom probe tomography analysis of oxide nanoparticles in metallic matrix: quantification and correction, J. Nucl. Mater. 492 (2017) 279–291, https://doi.org/10.1016/j.jnucmat.2017.05.008.
[36] W. Lefebvre, F. Vurpillot, X. Sauvage, Atom Probe Tomography - Put Theory into Practice, Elsevier Science, San Diego, 2016.
[37] C. Hatzoglou, B. Radiguet, F. Vurpillot, P. Pareige, A chemical composition correction model for nanoclusters observed by APT - application to ODS steel nanoparticles, J. Nucl. Mater. 505 (2018) 240–248, https://doi.org/10.1016/j.jnucmat.2018.03.057.
[38] V. Kuksenko, C. Pareige, C. Genevois, P. Pareige, Characterisation of Cr, Si and P distribution at dislocations and grain-boundaries in neutron irradiated Fe–Cr model alloys of low purity, J. Nucl. Mater. 434 (2013) 49–55, https://doi.org/10.1016/j.jnucmat.2012.11.027.
[39] V. Kuksenko, C. Pareige, P. Pareige, Cr precipitation in neutron irradiated industrial purity Fe–Cr model alloys, J. Nucl. Mater. 432 (2013) 160–165, https://doi.org/10.1016/j.jnucmat.2012.07.021.
[40] Z. Jiao, G.S. Was, Segregation behavior in proton- and heavy-ion-irradiated ferritic–martensitic alloys, Acta Mater. 59 (2011) 4467–4481, https://doi.org/10.1016/j.actamat.2011.03.070.
[41] J.P. Wharry, G.S. Was, A systematic study of radiation-induced segregation in ferritic–martensitic alloys, J. Nucl. Mater. 442 (2013) 7–16, https://doi.org/10.1016/j.jnucmat.2013.07.071.
[42] P. Auger, P. Pareige, S. Welzel, J.-C. Van Duysen, Synthesis of atom probe experiments on irradiation-induced solute segregation in French ferritic pressure vessel steels, J. Nucl. Mater. 280 (2000) 331–344, https://doi.org/10.1016/S0022-3115(00)00056-8.
[43] F. Gillemot, Á. Horváth, M. Horváth, A. Kovács, B. Radiguet, S. Cammelli, P. Pareige, M.H. Mayoral, A. Ulbricht, N. Kresz, F. Oszwald, G. Török, Microstructural changes in highly irradiated 15Kh2MFA steel, in: M. Kirk, E. Lucon (Eds.), Eff. Radiat. Nucl. Mater. 26th Vol, ASTM International, 100 Barr Harbor Drive, PO Box C700, West Conshohocken, PA, 2014, pp. 45–56, https://doi.org/10.1520/STP157220130098, 19428-2959.
[44] P. Efsing, J. Roudén, P. Nilsson, Flux effects on radiation induced aging behaviour of low alloy steel weld material with high nickel and manganese content, in: M. Kirk, E. Lucon (Eds.), Eff. Radiat. Nucl. Mater. 26th Vol, ASTM International, 100 Barr Harbor Drive, PO Box C700, West Conshohocken, PA, 2014, pp. 119–134, https://doi.org/10.1520/STP157220130112, 19428-2959.
[45] M.K. Miller, K.A. Powers, R.K. Nanstad, P. Efsing, Atom probe tomography characterizations of high nickel, low copper surveillance RPV welds irradiated to high fluences, J. Nucl. Mater. 437 (2013) 107–115, https://doi.org/10.1016/j.jnucmat.2013.01.312.
[46] P. Olsson, T.P.C. Klaver, C. Domain, *Ab initio* study of solute transition-metal interactions with point defects in bcc Fe, Phys. Rev. B 81 (2010), https://doi.org/10.1103/PhysRevB.81.054102.
[47] L. Messina, M. Nastar, T. Garnier, C. Domain, P. Olsson, Exact *ab initio* transport coefficients in bcc Fe – X (X = Cr , Cu , Mn , Ni , P , Si) dilute alloys, Phys. Rev. B 90 (2014), https://doi.org/10.1103/PhysRevB.90.104203.
[48] L. Messina, Multiscale Modeling of Atomic Transport Phenomena in Ferritic Steels, KTH Royal Institute of Technology, 2015.
[49] C.S. Becquart, R. Ngayam Happy, P. Olsson, C. Domain, A DFT study of the stability of SIAs and small SIA clusters in the vicinity of solute atoms in Fe, J. Nucl. Mater. 500 (2018) 92–109, https://doi.org/10.1016/j.jnucmat.2017.12.022.
[50] O. Tissot, C. Pareige, E. Meslin, B. Decamps, J. Henry, Kinetics of α′ precipitation in an electron-irradiated Fe15Cr alloy, Scripta Mater. 122 (2016) 31–35, https://doi.org/10.1016/j.scriptamat.2016.05.021.
[51] Z. Jiao, V. Shankar, G.S. Was, Phase stability in proton and heavy ion irradiated ferritic–martensitic alloys, J. Nucl. Mater. 419 (2011) 52–62, https://doi.org/10.1016/j.jnucmat.2011.08.020.
[52] O. Tissot, C. Pareige, E. Meslin, B. Décamps, J. Henry, Influence of injected interstitials on α′ precipitation in Fe–Cr alloys under self-ion irradiation, Mater. Res. Lett. 5 (2016) 117–123, https://doi.org/10.1080/21663831.2016.1230896.
[53] V. Kuksenko, C. Pareige, C. Genevois, F. Cuvilly, M. Roussel, P. Pareige, Effect of neutron-irradiation on the microstructure of a Fe–12at.%Cr alloy, J. Nucl. Mater. 415 (2011) 61–66, https://doi.org/10.1016/j.jnucmat.2011.05.042.

[54] P.D. Edmondson, S.A. Briggs, Y. Yamamoto, R.H. Howard, K. Sridharan, K.A. Terrani, K.G. Field, Irradiation-enhanced α′ precipitation in model FeCrAl alloys, Scripta Mater. 116 (2016) 112–116, https://doi.org/10.1016/j.scriptamat.2016.02.002.
[55] M. Bachhav, G. Robert Odette, E.A. Marquis, α′ precipitation in neutron-irradiated Fe–Cr alloys, Scripta Mater. 74 (2014) 48–51, https://doi.org/10.1016/j.scriptamat.2013.10.001.
[56] W.-Y. Chen, Y. Miao, Y. Wu, C.A. Tomchik, K. Mo, J. Gan, M.A. Okuniewski, S.A. Maloy, J.F. Stubbins, Atom probe study of irradiation-enhanced α′ precipitation in neutron-irradiated Fe–Cr model alloys, J. Nucl. Mater. 462 (2015) 242–249, https://doi.org/10.1016/j.jnucmat.2015.04.005.
[57] YuV. Konobeev, A.M. Dvoriashin, S.I. Porollo, F.A. Garner, Swelling and microstructure of pure Fe and Fe–Cr alloys after neutron irradiation to ~26dpa at 400°C, J. Nucl. Mater. 355 (2006) 124–130, https://doi.org/10.1016/j.jnucmat.2006.04.011.
[58] M.H. Mathon, Y. de Carlan, G. Geoffroy, X. Averty, A. Alamo, C.H. de Novion, A SANS investigation of the irradiation-enhanced α–α′ phases separation in 7–12 Cr martensitic steels, J. Nucl. Mater. 312 (2003) 236–248, https://doi.org/10.1016/S0022-3115(02)01630-6.
[59] E.R. Reese, M. Bachhav, P. Wells, T. Yamamoto, G. Robert Odette, E.A. Marquis, On α′ precipitate composition in thermally annealed and neutron-irradiated Fe- 9-18Cr alloys, J. Nucl. Mater. 500 (2018) 192–198, https://doi.org/10.1016/j.jnucmat.2017.12.036.
[60] F. Bergner, A. Ulbricht, C. Heintze, Estimation of the solubility limit of Cr in Fe at 300°C from small-angle neutron scattering in neutron-irradiated Fe–Cr alloys, Scripta Mater. 61 (2009) 1060–1063, https://doi.org/10.1016/j.scriptamat.2009.08.028.
[61] J.-H. Ke, E.R. Reese, E.A. Marquis, G.R. Odette, D. Morgan, Flux effects in precipitation under irradiation – simulation of Fe-Cr alloys, Acta Mater. 164 (2019) 586–601, https://doi.org/10.1016/j.actamat.2018.10.063.
[62] M. Bachhav, L. Yao, G. Robert Odette, E.A. Marquis, Microstructural changes in a neutron-irradiated Fe–6 at.%Cr alloy, J. Nucl. Mater. 453 (2014) 334–339, https://doi.org/10.1016/j.jnucmat.2014.06.050.
[63] A. Bhattacharya, E. Meslin, J. Henry, C. Pareige, B. Décamps, C. Genevois, D. Brimbal, A. Barbu, Chromium enrichment on the habit plane of dislocation loops in ion-irradiated high-purity Fe–Cr alloys, Acta Mater. 78 (2014) 394–403, https://doi.org/10.1016/j.actamat.2014.06.050.
[64] E.E. Zhurkin, D. Terentyev, M. Hou, L. Malerba, G. Bonny, Metropolis Monte-Carlo simulation of segregation in Fe–Cr alloys, J. Nucl. Mater. 417 (2011) 1082–1085, https://doi.org/10.1016/j.jnucmat.2010.12.191.
[65] L. Thuinet, M. Nastar, E. Martinez, G.F. Bouobda Moladje, A. Legris, F. Soisson, Multiscale modeling of Radiation Induced Segregation in iron based alloys, Comput. Mater. Sci. 149 (2018) 324–335, https://doi.org/10.1016/j.commatsci.2018.03.024.
[66] S. Novy, P. Pareige, C. Pareige, Atomic scale analysis and phase separation understanding in a thermally aged Fe–20at.%Cr alloy, J. Nucl. Mater. 384 (2009) 96–102, https://doi.org/10.1016/j.jnucmat.2008.10.008.
[67] G.R. Speich, A.J. Schwoeble, W.C. Leslie, Elastic constants of binary iron-base alloys, Metall. Trans. 3 (1972) 2031–2037, https://doi.org/10.1007/BF02643211.
[68] D. Terentyev, N. Juslin, K. Nordlund, N. Sandberg, Fast three dimensional migration of He clusters in bcc Fe and Fe–Cr alloys, J. Appl. Phys. 105 (2009) 103509, https://doi.org/10.1063/1.3126709.
[69] D. Terentyev, D.J. Bacon, YuN. Osetsky, Reactions between a 1/2 <111> screw dislocation and <100> interstitial dislocation loops in alpha-iron modelled at atomic scale, Philos. Mag. A 90 (2010) 1019–1033, https://doi.org/10.1080/14786430903019073.
[70] D. Terentyev, F. Bergner, Y. Osetsky, Cr segregation on dislocation loops enhances hardening in ferritic Fe–Cr alloys, Acta Mater. 61 (2013) 1444–1453, https://doi.org/10.1016/j.actamat.2012.11.021.
[71] G. Bonny, A. Bakaev, D. Terentyev, E. Zhurkin, M. Posselt, Atomistic study of the hardening of ferritic iron by Ni-Cr decorated dislocation loops, J. Nucl. Mater. 498 (2018) 430–437, https://doi.org/10.1016/j.jnucmat.2017.11.016.
[72] A.D. Whapham, M.J. Makin, The hardening of lithium fluoride by electron irradiation, Philos. Mag. A 5 (1960) 237–250, https://doi.org/10.1080/14786436008235839.
[73] G. Monnet, Multiscale modeling of irradiation hardening: application to important nuclear materials, J. Nucl. Mater. 508 (2018) 609–627, https://doi.org/10.1016/j.jnucmat.2018.06.020.
[74] G. Monnet, Multiscale modeling of precipitation hardening: application to the Fe–Cr alloys, Acta Mater. 95 (2015) 302–311, https://doi.org/10.1016/j.actamat.2015.05.043.
[75] R. Badyka, G. Monnet, S. Saillet, C. Domain, C. Pareige, Quantification of hardening contribution of G-Phase precipitation and spinodal decomposition in aged duplex stainless steel: APT analysis and micro-hardness measurements, J. Nucl. Mater. 514 (2019) 266–275, https://doi.org/10.1016/j.jnucmat.2018.12.002.